HEFAT2014
10th International Conference on Heat Transfer, Fluid Mechanics and Thermodynamics
14 – 16 July 2014
Orlando, Florida

Convergence of High-order Interpolation Schemes in Shear Layer Modelling

Karimpour Ghannadi S. and Chu Vincent H. *
Department of Civil Engineering and Applied Mechanics,
McGill University,
Montreal, Canada,
E-mail: Vincent.Chu@mcgill.ca

ABSTRACT

Capturing flow discontinuities and calculate energy dissipation across the shock wave correctly are challenging numerical simulation problem. Several highly accurate numerical interpolation schemes are employed to capture the shock waves developing in shear flow in shallow waters for two convective Froude numbers. The simulation starts from a small disturbance to the hyperbolic tangent (TANH) based velocity profile. The subsequent linear and nonlinear development of the shear instabilities are obtained from the numerical simulation using the second-order MINMOD, the third-order ULTIMATE-QUICK and the fifth-order WENO schemes. The computational error is evaluated using progressively smaller grid sizes. The number of nodes over a wave length are $\lambda/\Delta x = \lambda/\Delta y = 16$, 32, 64, 128, 256, and 512. The grid refinement determines the accuracy of the simulation and the order of convergence for each scheme. It also determines the dependence of the wave radiation and energy dissipation on the grid size.

INTRODUCTION

Instability analysis of the shear flow traditionally has been carried out using the linear stability analysis (LSA) and the normal mode approach (NNA). The initial growth of small disturbance is determined as an eigenvalue problem of the governing ordinary equations. Much has been studied on the linear instabilities in shallow waters using the NMA by Alavian & Chu [1], Chu et al. [2], Chen & Jirka [3][4] and Ghidaoui & Kolyshkin [5]. The nonlinear finite-amplitude development of the instabilities has to be determined from the numerical solution of the fully nonlinear equations. In this paper, the shear instabilities of transverse shear flow in shallow waters with the TANH base velocity profile is studied by numerical simulations using the shallow-water equations. The simulation reproduces the linear instabilities obtained from the NMA. It also provides the data for the nonlinear transition and therefore paves the way to a more details study of the turbulent flow.

Two series of simulations have been carried out. One series of simulations is conducted ignoring the sub-grid scale viscosity. The computations are then repeated to include the sub-grid viscosity in order to examine the role of the viscosity in the sub-grid scale modelling. Grid refinement studies are conducted to evaluate the performance of each scheme and to determine the role of sub-grid scale viscosity on linear and nonlinear development of the instabilities.

NOMENCLATURE

x	[m]	Cartesian axis direction
y	[m]	Cartesian axis direction
h	[m]	Water depth
q_x	[m^2/s]	Flow rate in the x-direction
q_y	[m^2/s]	Flow rate in the y-direction
u	[m]	Velocity in the x-direction
v	[m]	Velocity in the y-direction
ζ	[1/s]	Streamwise Vorticity

Special characters

τ_{ij}	[kg /s^2m]	Stress tensor
δ_ω	[m]	Vorticity thickness
δ_θ	[m]	Momentum thickness
Δ	[m/s]	Velocity difference across the shear layer
c	[m/s]	Gravity wave speed
H	[m]	Specific energy head
E	[m^3/s^2]	Energy density
P	[m^4/s^3]	Energy flux or radiation power
E	[m^3/s^3]	Rate of energy dissipation

Subscripts

uu	Upstream node of the upstream
u	Upstream node
c	Central node
d	Downstream node
dd	Downstream node of the downstream
1, 2	Side 1 and side 2 in the free streams
o	Initial condition

NUMERICAL METHOD

The numerical simulation for the shear instabilities is based on the finite volume approximation of the shallow-water equations:

$$\frac{\partial h}{\partial t}+\frac{\partial q_x}{\partial x}+\frac{\partial q_y}{\partial y}=0 \tag{1}$$

$$\frac{\partial q_x}{\partial t}+\frac{\partial}{\partial x}\left(\frac{q_x\,q_x}{h}\right)+\frac{\partial}{\partial y}\left(\frac{q_x\,q_y}{h}\right)=-\frac{1}{2}gh\frac{\partial h}{\partial x}+\frac{1}{\rho}\frac{\partial h\tau_{xx}}{\partial x}+\frac{1}{\rho}\frac{\partial h\tau_{xy}}{\partial y} \tag{2}$$

$$\frac{\partial q_y}{\partial t}+\frac{\partial}{\partial x}\left(\frac{q_y\,q_x}{h}\right)+\frac{\partial}{\partial y}\left(\frac{q_y\,q_y}{h}\right)=-\frac{1}{2}gh\frac{\partial h}{\partial y}+\frac{1}{\rho}\frac{\partial h\tau_{yy}}{\partial y}+\frac{1}{\rho}\frac{\partial h\tau_{yx}}{\partial x} \tag{3}$$

where h = flow depth, g = gravity, (u, v) = flow velocity, and $(q_x, q_y) = (uh, vh)$ = flow rate in the x- and y-direction, respectively. The base flow for the shear instability analysis is the hyperbolic tangent (TANH) velocity profile as shown in Figure 1. Simulations are carried out for two convective Froude numbers, Fr_c = 0.1 and 0.8. The convective Froude number is:

$$\mathrm{Fr}_c=\frac{U_1-U_2}{c_1+c_2} \tag{4}$$

In this expression for the convective Froude number, U_1 and U_2 are the free stream velocities in the longitudinal direction, and c_1 and c_2 are the wave speeds in the free streams. The governing equations in gas dynamics are similar in form and behaviour as the shallow-water equations [7]. The analogous shear instabilities in gas dynamics is the convective Mach number [8].

The numerical simulation begins with the introduction of a small perturbation (u', v', h') to the parallel base flow $[U(y), 0, H]$:

$$u=U(y)+u', v=v', h=H+h' \tag{5}$$

The subsequent development of (u', v', h') are calculated in a staggered grid using an implementation of the classical finite-volume method by Pinilla et al. [6]. The time integration of the shallow water equation (SWE) is made using the 4th-order Runge-Kutta method. Figure 2 shows the finite volumes for the continuity and momentum equations on the staggered grid. The values of h, q_x and q_y are defined at the h-node, q_x-node and q_y-node. The nonlinear fluxes on the faces of the finite volumes are: $\mathcal{F}^{uqx} = uq_x$, $\mathcal{F}^{vqx} = vq_x$, $\mathcal{F}^{uqy} = uq_y$, $\mathcal{F}^{vqy} = vq_y$, which are the sources of spurious numerical oscillations. Various flux limiting schemes have been introduced to control the numerical oscillations. Three representative schemes are considered in the present numerical simulations for the linear and nonlinear shear instabilities. These are (i) the second-order MINMOD scheme, (ii) the third-order ULTIMATE-QUICK scheme and (ii) the fifth-order WENO scheme.

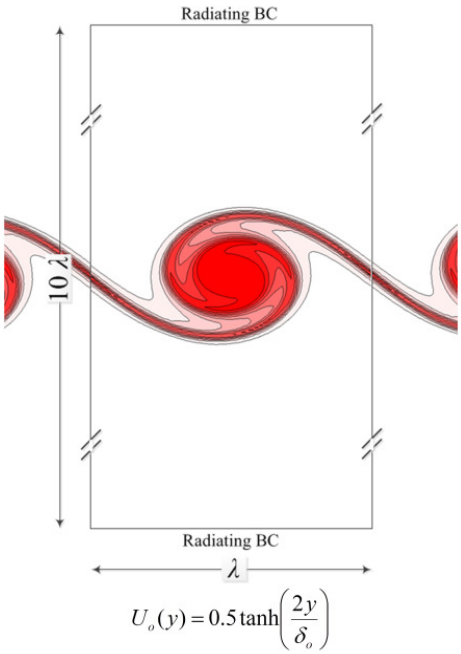

Figure 1 Schematic of temporal shear layer with periodic boundary condition in x-direction and radiating boundary condition in y-direction. The north and south radiating boundaries are 5λ away from the mixing layer.

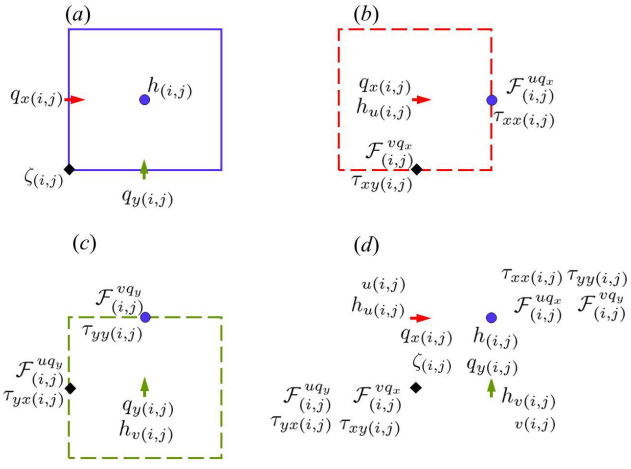

Figure 2 The finite volumes on the stagger grid for (a) the continuity equation, (b) the x-momentum equation, and (c) the y-momentum equation. The interpolations are needed for the four nodes shown in (d)

Interpolations are required in the staggered grid in order to evaluate the nonlinear fluxes at the h-node and ζ-node, and the depth h at the q_x-node and q_y-node as shown in Figure 2(d).

Flux Limiting Schemes

Spatial interpolation schemes of various accuracy and computational stability have been developed. High-order schemes, such as CD and QUICK, are accurate but are computationally unstable. To suppress spurious numerical oscillations, the fluxes are computed by flux limiting schemes. Some flux limiting schemes were introduced for Total Variation Diminishing (TVD) of the numerical oscillations [11]. Occasional downshifting to the diffusive lower-order scheme has been the strategy of many other flux limiting numerical schemes to gain computational stability [9][10][11][12][13]. The flux limiters suppress the spurious oscillations. It improves stability of the computation. It may as a consequence produce diffusion error which can be greater than the sub-grid scale viscosity employed in large-eddy simulation (LES) of turbulent flow [14][15].

Among the flux limiting schemes, the most diffusive is MINMOD. On the other hand, the WENO (Weighted Essentially Non-Oscillatory) scheme has the highest order of accuracy [16][17]. The implementation of the WENO scheme in this paper is fifth-order.

Grid Refinement Studies

The grid is refined over four stages. The numbers of the x-nodes over one wave length of the disturbance are N = 32, 64, 128 and 256 for the four stages of simulations of the flow with convective Froude number of Fr_c = 0.1. The number of x-nodes are N = 64, 128, 256 and 512 for the flow with the convective Froude number of Fr_c = 0.8. The higher degree of refinement of grid is selected for the higher Froude number in order to more correctly calculate the radiation of gravity waves from the shear instabilities.

Sub-grid Scale Viscosity

For the series of simulations including with the sub-grid scale model, the stresses are related to the strain rate through the sub-grid scale viscosity ν_{sg} as follows:

$$\tau_{ij} = \begin{vmatrix} \tau_{xx} & \tau_{xy} \\ \tau_{yx} & \tau_{yy} \end{vmatrix} = \rho \nu_{sg} \left(\frac{\partial u_i}{\partial x_j} + \frac{\partial u_j}{\partial x_i} \right) - \frac{1}{2} \rho \nu_{sg} \delta_{ij} \frac{\partial u_k}{\partial x_k} \qquad (5)$$

The sub-grid scale viscosity model proposed recently by Vreman [15] does not generate viscosity by the mean flow and therefore does not have the dissipative problem of the Smagorinsky model. The model was developed for three-dimensional (3D) turbulence simulation. The following expression of the sub-grid-scale viscosity is obtained from contraction of the 3D model for the present 2D simulation in open-channel shear flow:

$$\upsilon_{sg} = 2.5 C_s^2 \Delta^2 \sqrt{\frac{(a_{11}a_{22} - a_{12}a_{21})^2}{a_{11}^2 + a_{22}^2 + a_{12}^2 + a_{21}^2}} \qquad (6)$$

in which $a_{ij} = \partial u_j / \partial x_i$ is the deformation rate tensor. The value of the coefficient C_s = 0.2 originally proposed for 3D simulations is adopted for the present simulations of the 2D shear flow.

LINEAR INSTABILITY

The initial linear development of the small disturbance is exponential growth. The growth rate is determined by the fractional rate of the fluctuating velocity u' or by the v' as follows:

$$\alpha = \frac{\mathrm{d}[\ln u']}{\mathrm{d}t} = \frac{1}{u'} \frac{\mathrm{d}u'}{\mathrm{d}t} \qquad (7)$$

In practice however the growth rate is calculated as delineated in Figure 3 in terms of the kinetic energy of the disturbance K' = ½ (u'^2+ v'^2) as follows:

$$\alpha = \frac{\mathrm{d}[\ln K']}{\mathrm{d}t} = \frac{1}{2K} \frac{\mathrm{d}K'}{\mathrm{d}t} \qquad (8)$$

This formula is convenient because the value of K' is always positive.

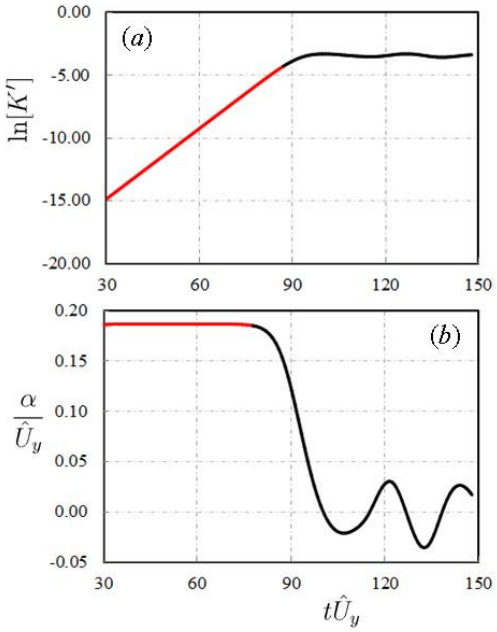

Figure 3 Variations of (a) the disturbance-kinetic-energy K' with time, and (b) the growth rate α with time, for wave number k = 0.8925 and convective Froude number Fr_c = 0.10. The initial linear development is delineated by the red-colour portion of the lines.

The numerical simulations have been carried for a range of wave length λ with the corresponding wave number varying from

$$k = \frac{2\pi\delta_{\omega_o}}{\lambda} = 0 \text{ to } 2 \tag{9}$$

The growth rate α were evaluated for two convective Froude numbers of Fr_c = 0.1 and 0.8. Figure 4 shows the dimensionless growth rate

$$\alpha^* = \frac{\alpha}{\hat{U}_y} \tag{10}$$

which is the rate normalized by the shearing rate at the inflection of the base flow velocity profile. The perturbation of the base flow of the TANH velocity profile is unstable over the range of wave number k = 0 to 2. The maximum rates of the exponential growth are α = 0.18747 and α = 0.07715 which occurs at the wave numbers k = 0.89250 and k = 0.50606 for the convective Froude numbers Fr_c = 0.1 and Fr_c = 0.8, respectively. Michalke [17] analyzed the shear instability of the mixing layer for incompressible flow (corresponding to a convective Froude number of Fr_c = 0) and found the dimensionless maximum growth rate to be α^* = 0.1898 occurs at the dimensionless wave number of k = 0.8892.

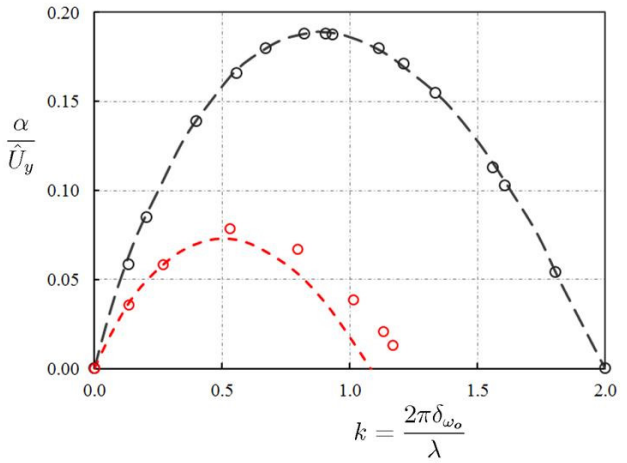

Figure 4 Instability diagram for dimensionless exponential growth rate α^* over the range of wave number k = 0 to 2 for two convective Froude numbers Fr_c = 0.1 and Fr_c = 0.8. The dashed lines are the instability relations obtained by Sandham & Reynolds [19] for shear flow in ideal gas with Mach number Ma = 0.1 and 0.8

Order of Convergence

The maximum growth rate occurs at k = 0.89 and 0.48 for Fr_c = 0.1 and 0.8, respectively. Simulations were conducted using progressively smaller grid sizes of Δx / λ = 1/512, 1/256, 1/128, 1/46 and 1/32. Figure 5 shows the order of convergence as the exponential rate approaches the exact solution.

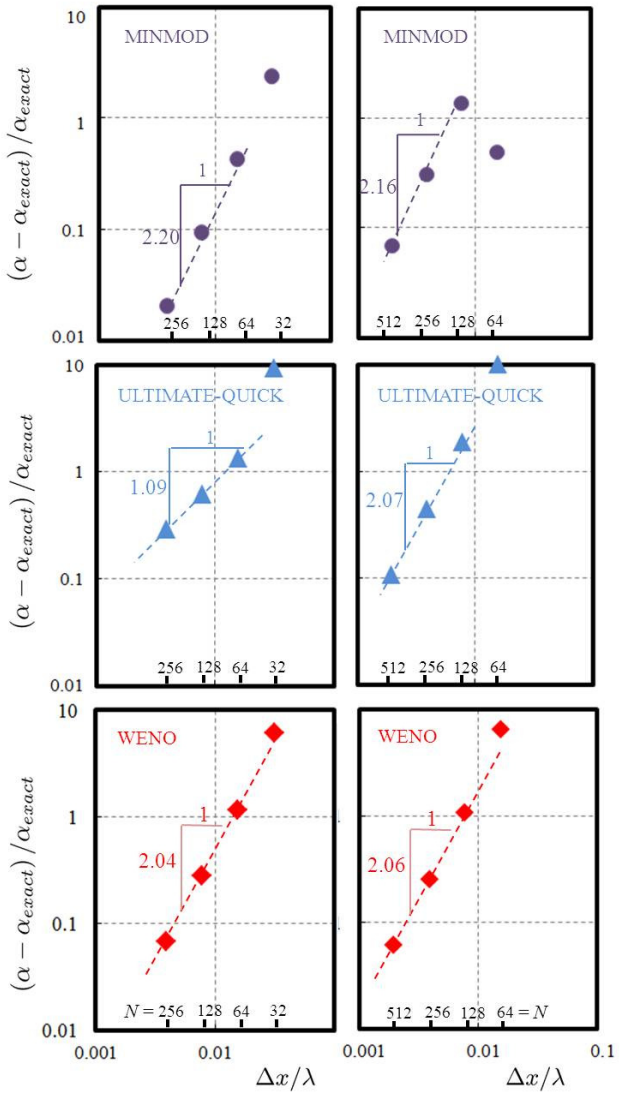

Figure 5 Fractional computational error for exponential growth rate, $(\alpha - \alpha_{exact}) / \alpha_{exact}$, obtained by MINMOD for (a) Fr_c = 0.1 and for (b) Fr_c = 0.8, ULTIMATE-QUICK for (c) Fr_c = 0.1 and for (d) Fr_c = 0.8 and WENO for (e) Fr_c = 0.1 and for (f) Fr_c = 0.8. The order of convergence for each scheme are determined using the progressively smaller grid sizes of Δx / λ = 1/512, 1/256, 1/128, 1/46 and 1/32.

NONLINEAR FINITE-AMPLITUDE DEVELOPMENT

As the disturbance grows exponentially, the small disturbance eventually becomes finite in amplitude. Figure 6(a) and 7(a) show the nonlinear growth rate of the finite amplitude disturbance for Fr_c = 0.1 and 0.8 respectively. In the non-linear stage the shearing rate at the inflection point of the mean profile

is time dependent. Figure 6(b) and 7(b) show the momentum thickness of the mean velocity profile determined by:

$$\delta_\theta = 2\int_0^\theta \frac{(U-U_1)(U-U_2)}{(U_1-U_2)^2}\,dy \qquad (11)$$

Another measure of the non-linear shear layer is the vorticity thickness:

$$\delta_\omega(t) = \frac{U_1-U_2}{\hat{U}_y(t)} \qquad (12)$$

These two thicknesses, δ_w and δ_θ are related approximately by a factor of 4. The point 1 in Figures 6 and 7 is the overshot of the growth rate immediately after the linear stage. Points 2, 3 and 4 are the zero crossing of the growth rate. Point 2 is the first peak of the momentum thickness in the non-linear stage of its development. Point 4 is the subsequent peak of its development.

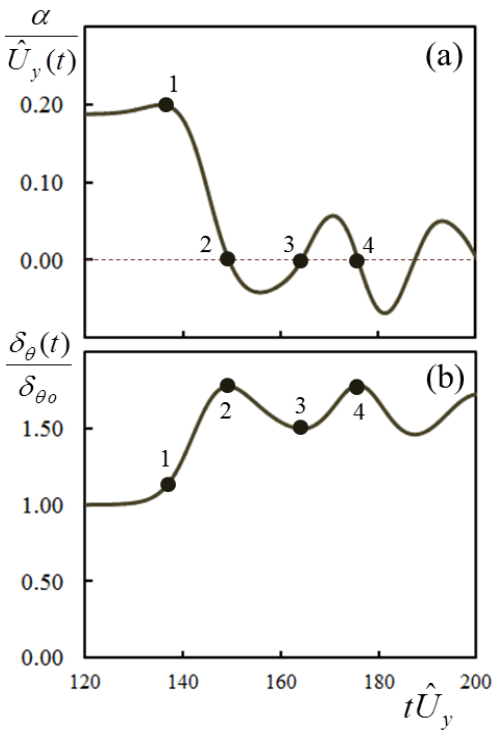

Figure 6 The (a) growth rate and (b) the momentum thickness in the non-linear development of the mixing layer for $Fr_c = 0.1$ using WENO reconstruction. Points 1 to 4 identify the non-linear growth stages.

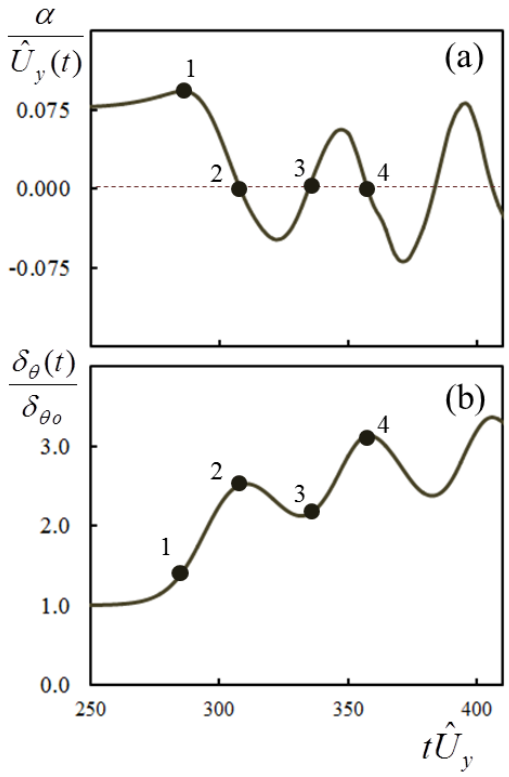

Figure 7 The (a) growth rate and (b) the momentum thickness in the non-linear development of the mixing layer for $Fr_c = 0.8$ using WENO reconstruction. Points 1 to 4 identify the non-linear growth stages.

The nonlinear development eventually leads to the formation of eddies for the lower convective Froude number of $Fr_c = 0.1$ as shown in Figure 8, and the formation of shocklet at the higher convective Froude number $Fr_c = 0.8$ as shown in Figure 8. The shocklets are characterized by the radiation of gravity waves and formation of shock waves (hydraulic jumps) within the shocklets. The most significant finding from the fully nonlinear simulation is the quasi-nonlinear oscillations of the eddies and shocklets as shown in Figures 8 and 9.

The development of the finite amplitude disturbance for the incompressible limit when Fr_c approaches zero has been examined by Stuart [19]. The solution obtained by Stuart known as Stuart's vortex, is a steady-state normal-mode approximation. The true solution is quasi steady. Using the fifth-order WENO scheme for the spatial interpolation, the quasi-steady oscillations are accurately calculated. The maximum-slope width $\delta_\omega(t)$ characterizing the dimensions of the eddy is a nearly periodic function of the time as shown in Figure 6.

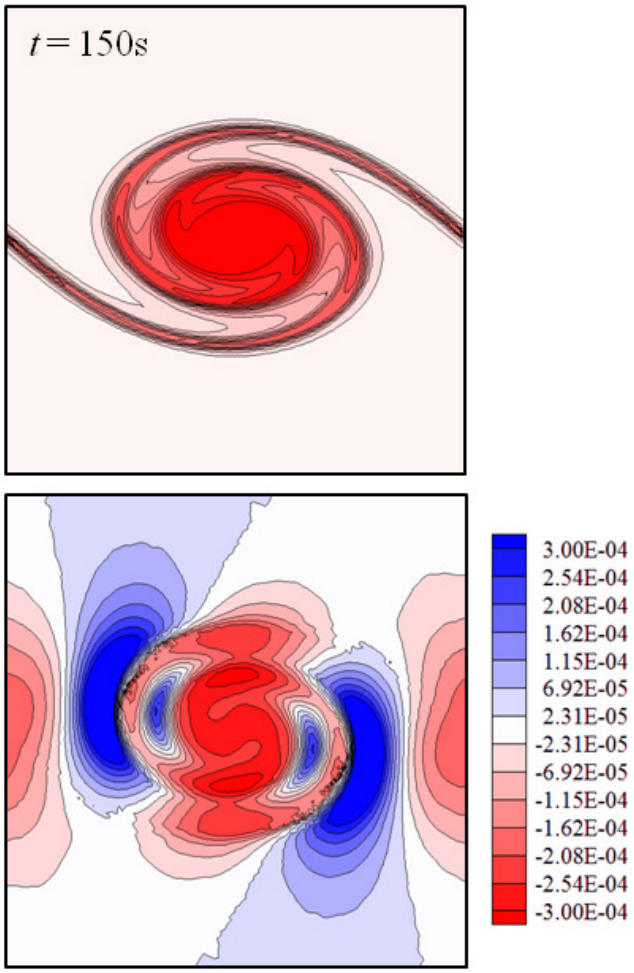

Figure 8 The vorticity contours showing the development of shear layers into eddies in shallow waters for the convective Froude numbers $Fr_c = 0.1$ at time of the first peak in the non-linear development of momentum thickness (at Point 2 in Figure 5) .

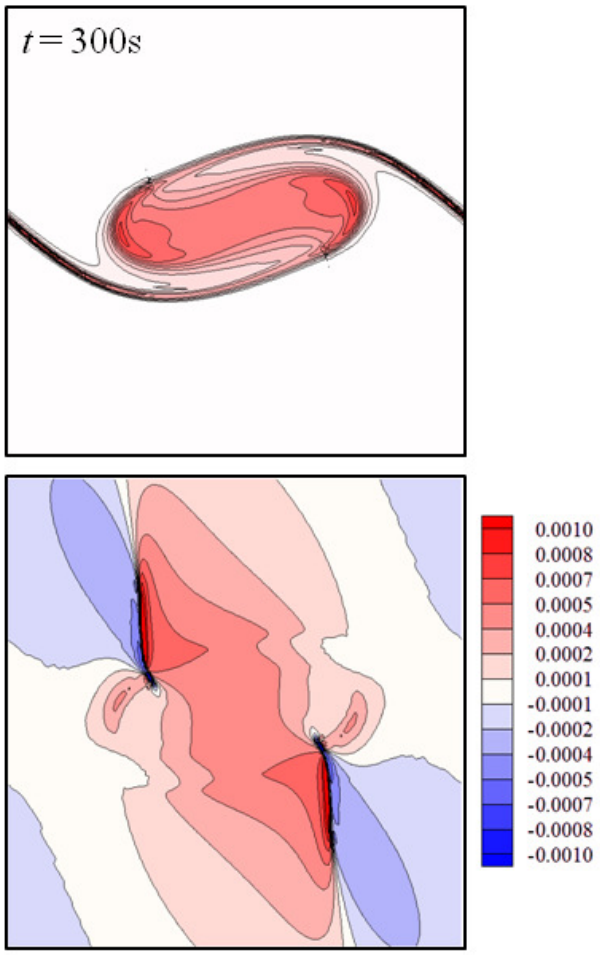

Figure 9 The vorticity contours showing the development of shear layers into eddies and shocklets in shallow waters for the convective Froude number $Fr_c = 0.8$ at time of the first peak in the non-linear development of momentum thickness (at Point 2 in Figure 6).

GRID REFINEMENT AND CONVERGENCE

Figure 10 shows the convergence of the vorticity thickness δ_ω toward its true solution $\delta_{\omega-exact}$. The 2nd-order TVD schemes such as MINMOD follow a lower order of convergence in compare with ULTIMATE-QUICK and WENO. The most accurate fifth-order WENO has the highest order of convergence. The ULTIMATE-QUICK is in between of the TVD schemes and the 5th-order WENO. The 2nd-order TVD schemes (MINMOD) have the lower order of convergence compared with the 5th-order WENO. A nearly 5th-order of convergence has been achieved by the simulation using the WENO scheme when the grid is sufficiently refined.

For the purpose of estimate the simulation error, the vorticity thickness δ_ω obtained in the first peak shown in Figure 6 and Figure 7 are used to determine the fraction error.

The fraction error is $(\delta_\omega - \delta_{\omega-exact})/\ \delta_{\omega-exact}$ and plotted in Figure 10 versus $\Delta x/\lambda$ for five levels of grid refinement. The number of nodes over one wave length in the computation are $\Delta x/\lambda$ = 512, 256, 128, 64, 32.

The grid refinement results for the fifth-order WENO is shown in Figure 10(a) and 10(b). In this case the order of convergence to the true solution is 4.42 and 4.20 for Frc = 0.1 and 0.8, respectively. Also included in Figure 9(a) is simulation results obtained using a sub-grid viscosity C_s = 0.2. Some what unexpected, the fractional error and the order of convergence is remarkably similar. The sub-grid viscosity appears to have no significant effect.

Figures 10(c), 10(d), 10(e) and 10(f) show the grid refinement results for the third-order ULTIMATE-QUICK and the second-order MINMOD. As expected these lower-order

schemes have higher fractional error and lower order of convergence.

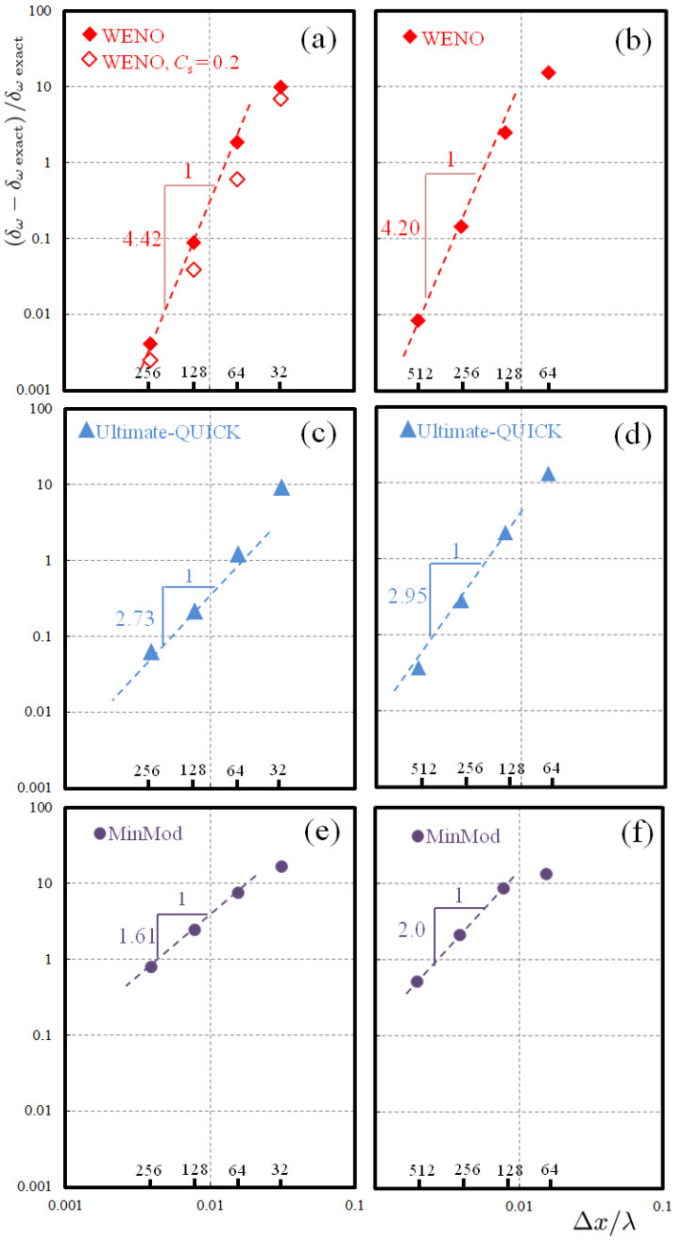

Figure 10 Fractional computational error for vorticity thickness, (δ_ω - $\delta_{\omega\ -exact}$) / $\delta_{\omega\ -exact}$, obtained by WENO for (a) Fr_c = 0.1 and for (b) Fr_c = 0.8, ULTIMATE-QUICK for (c) Fr_c = 0.1 and for (d) Fr_c = 0.8 and MINMOD for (e) Fr_c = 0.1 and for (f) Fr_c = 0.8. The order of convergence for each scheme are determined using the grid size of $\Delta x / \lambda$ = 1/512, 1/256, 1/128, 1/46 and 1/32. (at Point 2 in figure 5 and 6)

Formal calculations of the convergence factor R_k and the order of convergence P_k are by using the following formulae given by Stern et al. [19]. The formula for the convergence factor is

$$R_k = \frac{\delta_{k+1} - \delta_k}{\delta_k - \delta_{k-1}} \tag{13}$$

where δ_{k-1}, δ_k and δ_{k+1} are the simulation results obtained from the sequential refinement of the grid. The higher values of the index number k represent the greater degree of the grid resolution. The formula for the order of convergence and exact value estimation are:

$$P_k = \frac{\ln(\frac{\delta_k - \delta_{k-1}}{\delta_{k+1} - \delta_k})}{\ln(r)} \quad \text{where} \quad r = \frac{\Delta x_{k-1}}{\Delta x_k} \tag{14}$$

$$\delta_{exact} = \frac{r^p \delta_k - \delta_{k-1}}{r^p - 1} \tag{15}$$

where r is the grid refinement ratio and p is scheme order. The ratio is r = 2 for the present grid-refinement study. Figure 10 shows the calculations of the convergence factor and order of convergence obtained using these formulae for the simulation using the WENO, ULTIMATE-QUICK and MINMOD schemes. The convergence is monotonic for all schemes. The convergence order approaches a value of 1.61 and 2 for the MINMOD in Fr_c =0.1 and 0.8 respectively. It approaches values of 2.73 and 2.95 for ULTIMATE-QUICK, and a significantly higher value of 4.42 and 4.2 when the 5th-order WENO scheme was employed in the simulation.

ENERGY FLUX, RADIATION AND DISSIPATION

Highly accurate computational scheme is required to correctly calculate the energy dissipation across the shock waves. The calculation of energy dissipation is the balance of time rate of energy density and the divergence of energy flux. The derivation for the energy dissipation starts from the differential form of the energy equation:

$$\frac{\partial E}{\partial t} + \nabla \bullet P = 0 \tag{16}$$

. The terms are energy density

$$E = \frac{u^2 + v^2}{2} h + \frac{gh^2}{2} \tag{17}$$

and energy flux

$$P = \vec{u}h\left(\frac{u^2 + v^2}{2} + gh\right) \tag{18}$$

The integration of the above partial differential equation over an area of a control volume in two dimensions (2D) is:

$$\int_A \frac{\partial}{\partial t} E\, dA + \int_A \nabla \bullet P\, dA = 0 \tag{19}$$

where A is the volume per unit depth of the 2D control volume. The exchange of order between integration and differentiation leads to the energy dissipation, ε as given in the equation below:

$$\frac{\partial}{\partial t}\int_A E\, dA + \int_A \nabla \bullet P\, dA = \varepsilon \tag{20}$$

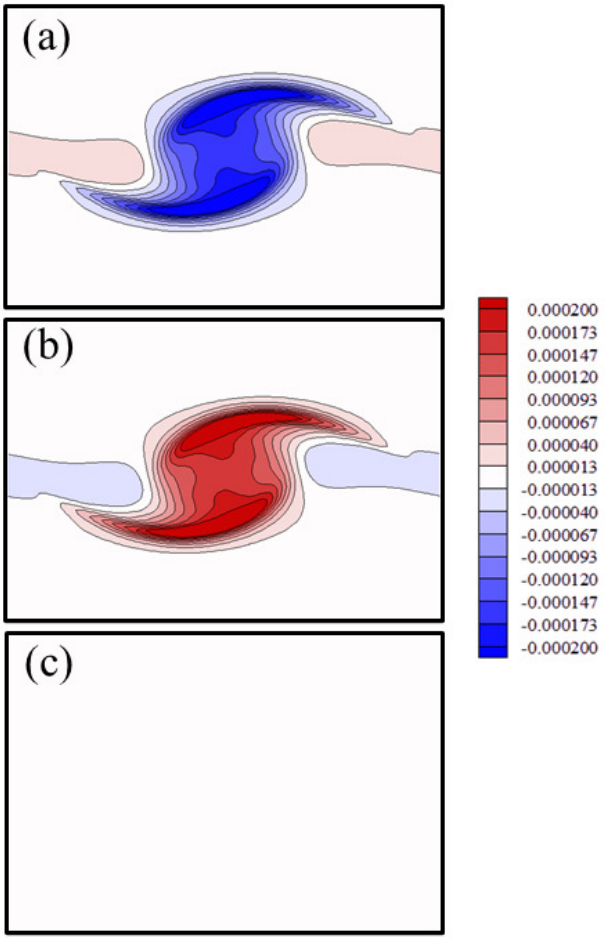

Figure 11 The energy-density rate (a), energy-flux divergence (b), and dissipation rate (c) as defined in Equation 20 from simulation for $Fr_c = 0.1$ at $t = 141$s.

There are terms in the energy equation, Equation 20. The first integral is the sum of energy density rate; the second integral is the sum of energy-flux divergence. The balance is the energy dissipation. The integrals are evaluated for each computational cell. Their distributions are shown in Figures 10 (a) and 10(b) for the convective Froude number of Fr_c = 0.1 and Figures 11(a) and 11(b) for Fr_c = 0.8. The energy dissipation rate ε for the flow of low Froude numbers is negligible, as it is indicated in Figure 11(c). The energy dissipation rate across the shock wave is significant for Fr_c = 0.8 as shown in Figure 12(c). Calculations shown in Figures 11 and 12 are carried out using the fifth-order WENO scheme with $\lambda/\Delta x = 128$ for $Fr_c = 0.1$ and $\lambda/\Delta x = 256$ for $Fr_c = 0.8$. These are the maximum grid size for energy dissipation to be calculated correctly. We have conducted energy dissipation calculation using coarser grid by other less accurate computational method and have found the results to be different. The relationship between grid size and the accuracy of energy dissipation calculations is complex and will be reported in greater details elsewhere.

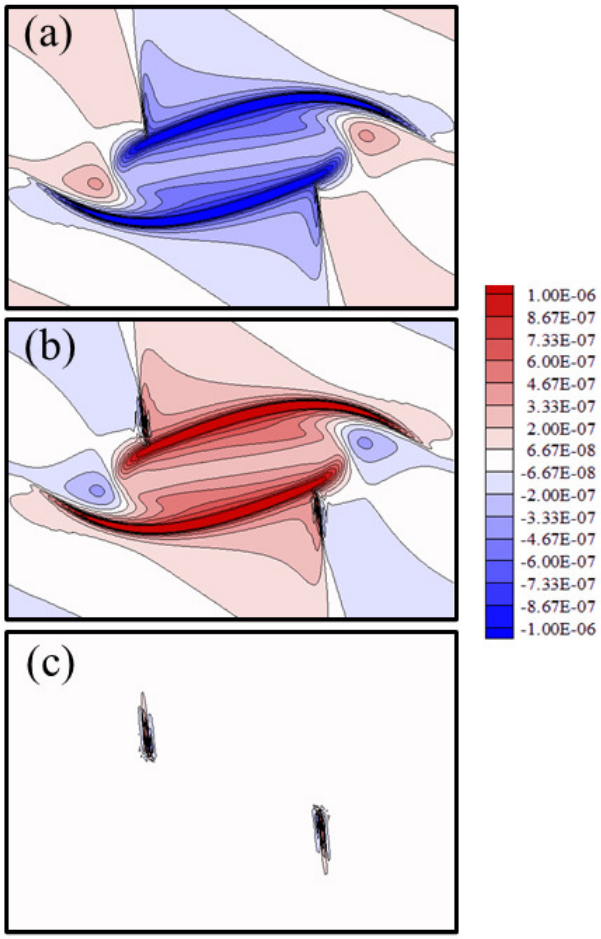

Figure 12 The energy-density rate (a), energy-flux divergence (b), and dissipation rate (c) as defined in Equation 20 from simulation for $Fr_c = 0.8$ at $t = 296$s.

To calculate the radiation from the shear instability, the energy equation is averaged over one wave length to give

$$\frac{\partial}{\partial t}\langle E\rangle + \frac{\partial}{\partial y}\langle P_y\rangle = \langle \varepsilon\rangle \tag{21}$$

where < > is the averaging operator defined by:

$$\langle E\rangle = \frac{1}{\lambda}\int_0^\lambda E\, dx, \quad \langle P_y\rangle = \frac{1}{\lambda}\int_0^\lambda P_y\, dx \tag{22}$$

In this equation, P_y is energy flux in the y-direction. Figures 13 and 14 show the average of the energy flux obtained at various locations in the lateral direction away from the shear instability. The energy flux is the power of radiation. It is oscillatory as the nonlinear instability that generate the radiation is oscillatory. The radiation power is observed in 16 stations located laterally each with a distance of 5λ/16 from the next station. The time-lag between the radiations represents the time it would take for the lateral wave to reach from one border to next. The time-lag for the gravity waves to travel one region is t_L=5λ/16c = 0.44s in case of Fr_c = 0.1. Therefore the time-lag from from region 1 to 16 is 6.6s. The time-lag for the gravity waves to travel one region is t_L=5λ/16c = 6.21s in case of Fr_c = 0.8. Therefore the time-lag from region 1 to 16 is 93.14s. Also the outflow of the power from region 16 is parallel to the predecessors proving that the radiating boundary is properly applied on this boundary.

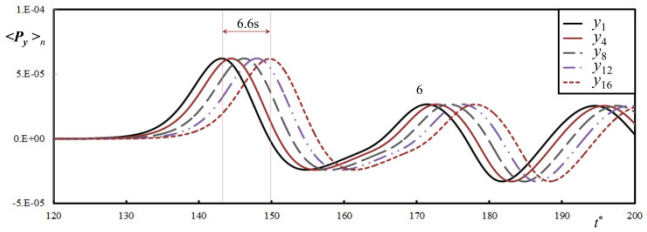

Figure 13 The power <P_y> radiated from the nonlinear instabilities; Frc = 0.1.

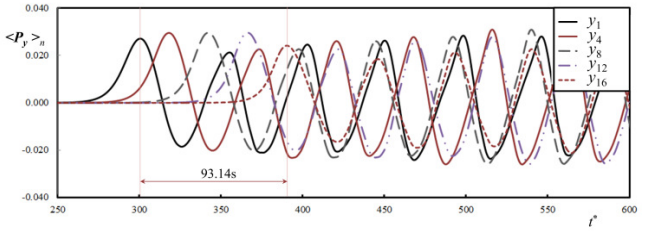

Figure 14 The power <P_y> radiated from the nonlinear instabilities; Frc = 0.8.

SUMMARY

Numerical computations of the shear instabilities in shallow waters were conducted using an accurate trans-critical solver for two convective Froude numbers. The nonlinear instabilities lead to the development of eddies as shown in Figure 8 and of shocklets in Figure 9. The radiation of waves from the instabilities and the formation of shock wave are responsible for the energy dissipation in the shear instability. The instabilities, the radiation and dissipation of energy in the shallow waters is analogous to the processes in gas dynamics [7][8]. The spurious numerical oscillations produced by the high-order spatial interpolation are managed by numerical schemes developed following the concept of minimal intervention [6]. The role of sub-grid viscosity and the accuracy of the numerical interpolation schemes are investigated for the nonlinear shear instabilities through multiple levels of grid refinement. Orderly and monotonic convergence to true solution is possible as the grid is progressively refined using 32, 64, 128, 256 and 512 nodes over one wave length of the instabilities. The most accurate interpolation method is WENO among the flux limiting schemes examined for the numerical accuracy.

CONCLUSION

Nonlinear shear instability is the precursor to turbulence. It is often not clear how false numerical diffusion may affect the turbulence simulations. To capture flow discontinuities, false numerical diffusion error can be significant as accuracy of the numerical scheme is reduced to first order. The sub-grid viscosity is second order [14][15]. Therefore, false numerical diffusion can potentially exceed the magnitude of the sub-grid scale viscosity [21]. The nonlinear simulations and the errors evaluated from the five levels of grid refinement are presented in this paper as a guide for the selection of grid in numerical simulation. The present study of the shear instability is part of a comprehensive investigation on the relative role and the interference between the false numerical diffusion error and the sub-grid scale viscosity in the modelling of turbulent flow.

REFERENCES

[1] Alavian, V. and Chu, V.H., Turbulent exchange flow in compound channel. *Proc. 21st IAHR Congress*, Melbourne, Australia, pp. 446-451, 1985.

[2] Chu, V. H., Wu, J.-H., Khayat, R.E.. Stability of transverse shear flows in shallow open channels. *J. Hydraulic Engineering*, Vol. 117(10), 1991, pp. 1-19.

[3] Chen, D. and Jirka, G.H., 1997. Absolute and convective instabilities of plane turbulent wakes in shallow water layer. *J. Fluid Mech*., Vol. 338, 1997, pp. 157-172.

[4] Chen, D. and Jirka, G.H., Linear instabilities of turbulent mixing layers and jets in shallow water layers. *J. Hydr. Res.*, Vol. 36, 1998, pp. 815-830.

[5] Ghidaoui, M.S. and Kolyshkin, A.A., Linear stability analysis of lateral motions in compound open channels. *J. of Hydraulic Engineering*, Vol. 125(8), 1999, pp. 871-880.

[6] Pinilla, C., Bouhairie, S., Tan, L.W. and Chu, V.H., Minimal intervention to simulations using the shallow-water equation, *J. Hydro-Environ. Res*., Vol. 3, part 4, 2001, pp. 201-207.

[7] Pinilla, C. and Chu, V.H., Waves and bed-friction effect on stability of transverse shear flow in shallow waters. *Journal of Coastal Research*, Vol 52, 2008, 207-214.

[8] Sandham, N. D., and W. C. Reynolds, Compressible mixing layer-Linear theory and direct simulation, AIAA journal, Vol. 28, 1990, pp. 618-624.

[9] Van Leer, B., Towards the ultimate conservative difference scheme III. Upstream-centered finite-difference schemes for ideal compressible flow, *J. Comp. Phys.*, Vol. 23 (3), 1977, pp 263-275.
[10] Harten, A., High resolution schemes for hyperbolic conservation laws. *J. Comput. Phys.*, Vol. 49, 1983, 357-93.
[11] Sweby, P.K., High resolution schemes using flux-limiters for hyperbolic conservation laws, *SIAM J. Num. Anal.*, Vol. 21 (5), 1984 , pp 995-1011
[12] Roe, P.L., Characteristic-based schemes for the Euler equations, *Ann. Rev. Fluid Mech*., Vol. 18, 1986, pp 337-365.
[13] Leonard, B.P. and Mokhtari, S., Beyond first-order upwinding: the ULTRA-SHARP alternative for non-oscillatory steady-state simulation of convection. *Int. J. Numerical Methods in Engrg.*, Vol. 30, 1990, pp 729-766.
[14] Smagorinsky, J., General circulation experiments with the primitive equations. I: the basic experiment, *Monthly Weather Review*, Vol. 91, 1963, pp 99-164.
[15] Vreman, A.W., An eddy-viscosity subgrid-scale model for turbulent shear flow: Algebraic theory and applications. *Physics of Fluids*. 16 (10), 2004, 3670-3681.
[16] Shu, C. W., High order weighted essentially non-oscillatory schemes for convection dominated problems. *SIAM Rev.*, Vol 51(1), 1998, pp 82-126.
[17] Shu C.W.. High order weighted essentially non-oscillatory schemes for convection dominated problems. *SIAM* Review, 51: 82-126, 2009.
[18] Michalke, A., On the inviscid instability of the hyperbolic-tangent velocity profile. Journal of Fluid Mechanics, Vol. 19, 1964, pp. 543-556.
[19] Sandham, N.D. and Reynolds, W.C., Compressible mixing layer: linear theory and direct simulation. AIAA Journal, v. 28, n. 4, 1990, pp. 618-624.
[20] Stuart, J. T., On finite amplitude oscillations in laminar mixing layers. *J. Fluid Mech*., Vol. 29, 1967, pp 417-440.
[20] Stern, F., Wilson, R.V., Coleman, H.W., Paterson, E.G., Comprehensive approach to verification and validation of CFD simulations—Part 1: methodology and procedures. *J. Fluids Eng.,* Vol 123(4), 2001, pp793-802.
[21] Chu, V.H. and Gao, C., False diffusion produced by flux limiters, *Computational Thermal Sciences*, Vol. 5(6), 2013, pp. 503-520.